# One-pot synthesis of nano-crystalline MCM-22

Christiaan H. L. Tempelman[1], M. Teresa Portilla[2], Marta E. Martínez-Armero[2], Brahim Mezari[1], Niek G.R. de Caluwé[1], Cristina Martínez[2], Emiel J. M. Hensen[1,*]

[1] Laboratory of Inorganic Materials Chemistry,

Schuit Institute of Catalysis, Eindhoven University of Technology,

Den Dolech 2, 5612 AZ Eindhoven, The Netherlands

[2] Instituto de Tecnología Química (UPV-CSIC), Universidad Politécnica de Valencia,

Consejo Superior de Investigaciones Científicas, Av. de los Naranjos s/n,

Valencia, 46022, Spain

Corresponding author: E.J.M. Hensen

E-mail: e.j.m.hensen@tue.nl

Tel: +31-40-2475178

Abstract

Nano-crystalline MCM-22 zeolite was synthesized in a one-pot procedure by the use of an organosilane (*dimethyl-octadecyl-(3-trimethoxysilylpropyl)-ammonium chloride*, TPOAC) in the zeolite synthesis gel. This crystal growth inhibition procedure introduced mesopores in the MCM-22 crystallites. The lower mechanical stability of the nano-crystalline MCM-22 zeolite compared with bulk MCM-22 can be countered to some extent by pillaring. The increased external surface of the microporous zeolite domains resulted in increased accessibility of the Brønsted acid sites, as followed from the better performance in liquid-phase benzene alkylation with propylene as compared with bulk MCM-22. The increased accessibility of the internal acid sites in Mo-loaded hierarchical MCM-22 was also evident from the improved benzene selectivity during methane aromatization. Silylation of hierarchical Mo/MCM-22 was detrimental for the catalytic performance in MDA. The nano-crystalline MCM-22 has physico-chemical and catalytic properties intermediate between those of MCM-22 and ITQ-2 with the benefit over ITQ-2 that it can be synthesized in a single step.

Keywords: MCM-22, mesopore, organosilane, benzene alkylation, methane aromatization

## 1. Introduction

Since the first report in the early 1990s [1], MCM-22 zeolite has attracted considerable attention of the catalysis community. MCM-22 is a medium-pore zeolite, prepared at typical Si/Al ratios between 10 and 20. The MWW pore topology endows promising catalytic properties to MCM-22 zeolites. For instance, MCM-22 exhibits shape selectivity properties in the trans-alkylation of toluene to *p*-xylene [2]. Its potential for the hydroisomerization of *n*-alkanes into branched alkanes [3, 4] and the alkylation of benzene to cumene and ethylbenzene [5, 6, 7] has also been demonstrated. MCM-22 has also been explored as an acidic support in methane dehydroaromatization [8, 9].

As-synthesized MCM-22 consists of MWW layers that are kept together by hydrogen bonds between the silanol groups that terminate the layers. Calcination of this precursor leads to condensation of these silanol groups, resulting in a rigid crystal. The micropore system of MCM-22 is made up from two separate two-dimensional channel systems [1]. The micropore channels in the [001] direction consist of straight 10-membered rings with a diameter of typically 5.6 Å [1, 10]. The second pore system is created when two cups located at the surface of adjacent MWW layers are connected to form a supercage. These large ellipsoidal cages are typically 7.1 Å in diameter and 18.2 Å in height [10]. The large cages are connected with each other through 10-membered ring windows.

MCM-22 is employed at the industrial scale for the liquid-phase alkylation of benzene to cumene and ethylbenzene [11-13]. The application of a solid catalyst such as MCM-22 for benzene alkylation is important, because it can replace environmentally stressing $AlCl_3$ [14]. Sastre *et al.* have shown that benzene does not enter the micropores of MCM-22 under liquid-phase conditions, which has been related to the slightly twisted micropore entrances

[15]. Accordingly, it has been assumed that alkylation takes mainly place over Brønsted acid sites (BAS) located at the external surface of MCM-22. In agreement with this, increasing the external surface by delamination improves the catalytic performance in alkylation reactions [5, 16]. Delaminated MCM-22 (ITQ-2) consists of single MWW layers and contains a high concentration of surface BAS, which are accessible to relatively bulky molecules [5]. The preparation of ITQ-2 involves a number of delicate steps, including swelling of as-synthesized MCM-22 by a surfactant, delamination by ultra-sonication and hydrolysis [17].

One of the other possible uses of MCM-22 zeolite is as the acidic component in bifunctional catalysts for non-oxidative methane dehydroaromatization (MDA). This reaction converts methane into benzene and hydrogen. The most studied catalyst for this reaction is Mo/ZSM-5 [18], although also other zeolite types - mainly medium pore structures - have been tested. Several studies report that MCM-22 zeolite performs better than ZSM-5 [19-21]. MDA catalysts are comprised of an acidic zeolite and Mo-oxide. The Mo-oxide precursor supported on the zeolite is rapidly converted into Mo-carbide under reaction conditions. These Mo-carbide particles convert methane into a $C_2$-intermediate, presumably ethylene, which is further converted over BAS into benzene, toluene and naphthalene. The main challenge to further develop the MDA technology is to overcome the rapid deactivation of the catalyst by coke formation [22-26]. Decreasing the crystal size has been shown to lower the deactivation rate for Mo/ZSM-5 and Mo/MCM-22 catalysts [27-29].

A large number of methods to synthesize hierarchically structured zeolites have been described along the last decade. A number of reviews categorize and discuss these

approaches [30-32]. Broadly speaking, two strategies can be followed, namely bottom-up and top-down approaches. In top-down approaches, mesopores are introduced after the zeolite has been synthesized, and it is usually achieved by extracting either Al or Si atoms from the zeolite framework. Common methods for demetallation include steaming [33-40], acid-leaching [30-46] and base treatment [47, 48]. In bottom-up approaches, the mesopores are introduced in the framework during the synthesis. This approach usually involves the use of a space-filling molecule (mesoporogens). For example, mesoporous voids can be introduced by the simple addition of carbon beads to the synthesis gel of MFI [49-51]. Choi *et al*. were the first to report the introduction of intra-crystalline mesoporosity using an amphiphilic organosilane surfactant molecule (dimethyl-octadecyl-(3-trimethoxysilylpropyl)-ammonium chloride, TPOAC) [41]. Recently, Carvalho *et al*. have prepared nano-crystalline ZSM-12 by this approach [42]. In contrast to MFI for which several direct routes for hierarchical structuring have been explored, only one route has been reported for the preparation of hierarchical MCM-22. This route involves the addition of carbon black pearls to the synthesis gel [29, 52].

In this study, we report about a one-pot synthesis approach of nano-crystalline MCM-22 by use of TPOAC as a crystal growth inhibitor. The addition of TPOAC impedes the crystallite growth, in a similar manner as has been shown for nano-crystalline ZSM-12 [42]. The mechanical stability of this nano-crystalline MCM-22 zeolite can be improved by pillaring. The resulting zeolite material shows improved performance in the liquid-phase alkylation of benzene and the aromatization of methane compared to catalysts based on bulk MCM-22.

## 2. Experimental

### *2.1 Synthesis of materials*

A literature procedure was employed for the preparation of bulk MCM-22 [53]. This recipe was modified to generate mesoporosity by adding an organosilane. In a typical synthesis, an amount of 5.85 g silica gel (Sigma Aldrich) was mixed with 2.97 g of hexamethylene imine (HMI) in a round-bottom flask. In a second round-bottom flask, 0.385 g sodium hydroxide and 0.48 g sodium aluminate were dissolved in 30 ml water. The latter solution was added to the first one and the mixture was stirred overnight at room temperature. Then, dimethyl-octadecyl-(3-trimethoxysilylpropyl)-ammonium chloride (60 wt% in methanol, ABCR) was added and the stirring was continued for 4 h. The resulting gel was transferred to a Teflon-lined stainless-steel autoclave and kept at 423 K for 7 days under rotation (60 rpm). The Si/Al ratio of the final synthesis gel was 16.3. The HMI/TPOAC ratio in the synthesis gel was varied (HMI/TPOAC = 6, 12 and 120). The resulting solids are denoted as MCM-22(*x*) with *x* being the HMI/TPOAC ratio. MCM-22 prepared without TPOAC in an otherwise similar synthesis gel served as the reference. The organics were removed from the as-synthesized materials using calcination in artificial air (20/80 (v/v) $O_2$/He) at 623 K for 6 h using a heating rate of 1 K/min.

Silica pillars were introduced in MCM-22 by impregnating 1 g of the non-calcined MCM-22(12) with 4 g of tetrapropylammonium hydroxide solution (40 wt% TPOAH). The suspension was stirred for 16 h at room temperature. To 1 g of the resulting zeolite/TPOAH mixture, 5 g of tetraethylorthosilicate (TEOS) was added under vigorous stirring in Ar atmosphere. This mixture was stirred at 351 K for 25 h. This procedure was followed by addition of HCl until the pH was 1. The resulting mixture was stirred for 6 h at 313 K. The

solid was recovered by filtration and washed with copious amounts of water. The material was dried overnight at 373 K and finally calcined. Calcination was done by heating in $N_2$ atmosphere to 723 K followed by exposure to artificial air (20/80 (v/v) $O_2$/He) at 823 K for 12 h. The pillared sample was denoted as MCM-22(12)-pillared.

Another reference sample was ITQ-2. This delaminated zeolite was prepared following the procedure outlined by Corma and co-workers [54]. As-synthesized MCM-22 was used as the starting material for the delamination procedure. To 1 g of the MCM-22 precursor 3.9 ml of CTAB solution (29 wt%, CTAB) was added. After dispersion 1.2 g TPAOH (40 wt% in water) was added. The final mixture was heated for 16 h at 353 K. After this, the mixture was ultrasonicated for 1 h. Finally, the pH was adjusted to 2 and stirred for 1 h and subsequently filtered. To remove the organic constituents the solid was calcined in artificial air at 823 K for 6 h.

To obtain the proton form, the zeolites were ion-exchanged in a 1 M $NH_4NO_3$ solution for 4 h followed by filtration. This procedure was repeated two times. After drying overnight at 383 K, the solids were calcined at 723 K for 4 h in an artificial air flow.

For methane dehydroaromatization, molybdenum was loaded onto the MCM-22 zeolites. For this purpose, the dried zeolite was impregnated with a solution of appropriate concentration ammonium heptamolybdate tetrahydrate (AHM, Merck). After impregnation the samples were dried for 1 h. The targeted Mo content was 4 wt%. The Mo-loaded zeolites were calcined in artificial air after heating to 823 K at a rate of 1.5 K/min. The final temperature and the dwell time at this temperature were varied. Zeolites modified with molybdenum are denoted by the prefix “Mo/”.

A portion of the Mo-modified zeolites was silylated by a procedure described in the literature [55]. For this purpose, 2 g of zeolite was dried at 373 K overnight and then dispersed in 50 ml n-hexane. To this suspension, 0.3 ml tetraethylorthosilicate (TEOS, Merck) was added under stirring and, subsequently, refluxed for 1 h. The amount of TEOS corresponded to 0.4 wt% based on the amount of zeolite in the suspension. Thereafter, the catalyst was filtered and dried at 373 K overnight. Finally, the zeolite was calcined in two steps. The first step consisted of heating the sample at a rate of 2 K/min to 393 K followed by an isothermal period of 2 h. The second step further increased the temperature to 773 K at a rate of 0.2 K/min followed by an isothermal period for 4 h. The silylation treatment was denoted by adding "Si" to the catalyst notation, e.g., Mo/MCM-22(12, Si).

*2.2 Characterization*

XRD patterns were recorded on a Bruker D4 Endeavor machine using Cu Kα radiation. Diffraction patterns were measured in the $5° \leq 2\Theta \leq 60°$ range using a step size of 0.1°.

Ar sorption isotherms were measured at 87 K on a Micromeritics ASAP2020 system in static measurement mode. The samples were outgassed at 623 K for 8 h prior to the sorption measurements. The Brunauer–Emmett–Teller (BET) equation was used to determine the surface area ($S_{BET}$) from the adsorption data in the $p/p_0 = 0.05–0.25$ range. The mesopore volume ($V_{meso}$) and mesopore size distribution were determined by applying the Barrett–Joyner–Halenda (BJH) method to the adsorption branch of the isotherm. The micropore area ($S_{micro}$) and micropore volume ($V_{micro}$) were calculated by the NLDFT method (Ar at 87 K on oxides as the model, assuming cylindrical pores, without regularization).

Infrared spectra were recorded in the 4000-400 $cm^{-1}$ range using a Bruker Vertex 70v apparatus. Samples were pressed into a self-supporting wafer with a density of about 10 $mg/cm^2$. To remove adsorbed water the sample was evacuated for 2 h at 773 K. After evacuation the sample was cooled to 323 K followed by recording of the background spectrum. The BAS concentration was determined by measuring IR spectra of adsorbed pyridine. Pyridine adsorption was carried out on the dehydrated zeolite wafer at 423 K. After saturation was reached following exposure to gaseous pyridine, the sample was evacuated at 523 K for 2 h and a spectrum was recorded. The evacuation step was repeated at 623 K and 673 K. The acidity of the samples was determined by deconvolution of the weight normalized spectra according standard procedures and the obtained values are expressed in arbitrary units.

Magic-angle spinning (MAS) nuclear magnetic resonance (NMR) measurements were performed on a 11.7 T Bruker DMX500 NMR spectrometer operating at a frequency of 500 MHz for $^{1}H$ measurements. The $^{27}Al$ MAS NMR spectra were measured using a Bruker 2.5-mm MAS probehead spinning at 20 kHz. The $^{1}H$ and $^{29}Si$ MAS NMR measurements were carried out using a 4-mm MAS probehead at sample rotation rates of 12.5 kHz for $^{1}H$ and 10 KHz for $^{29}Si$ NMR measurements, respectively.

Quantitative $^{1}H$ NMR spectra were recorded with a Hahn-echo p1-τ1-p2-τ2-aq pulse sequence with a 90º pulse with p1 = 5 μs and a 180º pulse with p2 = 10 μs. The interscan delay was set at 120 s. Quantitative $^{29}Si$ NMR spectra were recorded using a high power proton decoupling direct excitation (DE) pulse sequence with a 45 º pulse duration of 2.5 μs and an interscan delay of 160 s. $^{1}H$-$^{29}Si$ cross-polarization (CP) spectra were obtained using an interscan delay of 3 s and a contact time of 3 ms. $^{27}Al$ NMR spectra were recorded

with a single pulse sequence with a 180$^{o}$ pulse duration of 1 μs and an interscan delay of 1 s. $^{1}$H and $^{29}$Si NMR shifts were referred to tetramethylsilane (TMS), while saturated $Al(NO_3)_3$ solution was used for $^{27}$Al NMR shift calibration. For $^{1}$H MAS NMR measurements, the zeolites were first dehydrated at a temperature of 723 K at vacuum lower than $10^{-5}$ mbar for 6 h. The dehydrated zeolites were placed into the 4 mm MAS NMR zirconia rotor under inert conditions. The deconvolution of the NMR spectra was done using DMfit2011.

Transmission electron micrographs were obtained with a FEI Tecnai 20 transmission electron microscope (TEM) at an electron acceleration voltage of 200 kV. Typically, a small amount of sample was suspended in ethanol, sonicated and dispersed over a Cu grid with a holey carbon film. Scanning electron microscopy (SEM) was performed using a Philips environmental FEIXL-30 ESEM FEG in high-vacuum mode at low voltage.

*2.3 Catalytic activity measurements*

The catalytic activity in the alkylation of benzene with propylene was evaluated in a high-pressure stainless-steel reactor at 398 K and 3.5 MPa. For these measurements, the zeolites were pelletized, crushed and sieved in a 0.25–0.42 mm fraction, and diluted with silicon carbide to a total bed volume of 3.6 ml. The molar benzene/propylene ratio in the feed was 3.5. The weight-hourly space velocity (WHSV) was 25 $h^{-1}$ to the olefin in the feed. Samples were analyzed as a function of time on stream by online gas chromatography (5% phenyl–95% dimethylpolysiloxane column, length 30 m, internal diameter of 0.25 mm, 1 μm thick stationary phase film).

The catalytic performance of Mo-loaded zeolites in methane dehydroaromatization was measured in a fixed-bed reactor at 973 K, 0.1 MPa and a contact time of 16 g cat·h/mol $CH_4$ (GHSV = 1500 $h^{-1}$). The catalyst weight was 0.5 g, and was diluted with silicon carbide to achieve a bed volume of 2.8 $cm^3$. We verified that the diluent was not catalytically active. Prior to reaction, the catalysts were heated from room temperature to 973 K at a heating rate of 10 K/min in a methane/nitrogen mixture (80 vol% methane). After reaching the reaction temperature, the reactor was purged with $N_2$ for 0.5 h. Finally, the feed was switched to methane. The reactor outlet was analyzed by a two-channel online gas chromatograph. $N_2$ used as internal standard, $H_2$, CO, $CO_2$ and $CH_4$ were separated over HayeSep N (0.5 m), HayeSep Q (1.5 m) and 13X molecular sieve (1.2 m length) columns (TCD). In the second channel, hydrocarbons were separated over a pre-column (CP-Wax capillary column, 5.0 m length and 0.32 mm inner diameter). The light hydrocarbon products were further separated in a CP-Porabond Q (25 m length and 0.32 mm inner diameter) and detected by a FID. The aromatics were detected by FID after separation over a CP-Wax column (1.0 m length and 0.32 mm inner diameter).

## 3. Results and discussion

### 3.1 Preparation, characterization and catalytic testing of acid zeolites.

*Acid catalyst preparation and physico-chemical properties*

The XRD patterns of the as-prepared MCM-22 zeolites are shown in Fig. 1. MCM-22, MCM-22(12) and MCM-22(120) have the MWW structure [53], but the diffraction peaks are less intense and broader for the materials prepared at lower HMI/TPOAC ratio. The material prepared at a HMI/TPOAC ratio of 6 was almost completely X-ray amorphous. The ITQ-2 reference material was obtained by exposing as-synthesized MCM-22 (MCM-22(p)) to a delamination step followed by calcination. The XRD pattern of ITQ-2 matches the one given in the literature [56]. Table 1 shows that the Si/Al ratios of the MCM-22 materials prepared with and without TPOAC are similar. The textural properties of the crystalline materials were determined by Ar physisorption and the results are listed in Table 1. The micropore volume of MCM-22 was 0.15 $cm^3/g$, in good agreement with literature values [57]. The use of TPOAC led to a small decrease in the micropore volume. The mesopore volume increased with decreasing HMI/TPOAC ratio. The zeolite prepared at a HMI/TPOAC ratio of 12 had the largest mesopore volume ($V_{meso}$ = 0.3 $cm^3/g$). The higher surface area of ITQ-2 compared with bulk MCM-22 (414 $m^2/g$ *vs.* 117 $m^2/g$) indicates that MCM-22(p) was delaminated to a significant extent. Still, the surface area of our ITQ-2 is lower compared with some of the values reported before for this material starting from laminar precursors prepared with higher Si/Al ratios [58]. The lower surface area of our ITQ-2 material is likely due to the difficulty of delaminating MCM-22(p) with relatively high Al content (Si/Al ratio ~15) [58].

In general, the mechanical stability of hierarchical zeolites is lower than that of bulk zeolites and exerting mechanical forces usually reduces the beneficial mesoporosity. Pillaring is an established procedure to increase the mechanical stability of such hierarchical zeolites [59]. In the present work, we applied this procedure to MCM-22(12) because of its favorable textural properties. Comparison of the XRD patterns before and after pillaring (Fig. 1) shows that the crystallinity was not affected. Ar physisorption data point to the substantial decrease of the micropore volume due to pillaring, suggesting that part of the micropores were blocked due to deposition of TEOS in the micropores. The textural properties were also determined after pressing bulk MCM-22, MCM-22(12) and pillared MCM-22 (Fig. 2). Comparison of the Ar sorption isotherms before and after pressing the samples shows that the decrease of the mesopore volume upon mechanical stress was lower for MCM-22(12)-pillared than for MCM-22(12). This is particularly evident from the decrease of the hysteresis loop. On contrary, the isotherm of bulk MCM-22 is hardly affected by the pressing procedure. All this is also evident from the textural data derived from the Ar physisorption isotherms listed in Table 1. It is interesting to note that the mechanical stability test led to a decrease of the micropore volume of MCM-22(12) and MCM-22, but not for the pillared zeolites.

The morphology of these zeolites was investigated by electron microscopy. Representative SEM images are shown in Fig. 3. The primary crystals of MCM-22 show the well-known platelet morphology of MWW zeolite arranged in larger spherical secondary particles. The crystal size of these platelets is several nanometers. From SEM, the morphology of MCM-22(12) and MCM-22(12)-pillared appears to be more open. The morphology of ITQ-2 is

also platelet-like, arranged in a more aligned fashion, likely due to the single layer morphology at the nano-scale.

Fig. 4 depicts representative TEM images of the same materials. The thickness of the MWW crystallites for MCM-22(12) (Fig. 4b), which are in the range of 30-40 nm, are seen to be similar to MCM-22 (Fig. 4a). More detailed inspection of the TEM images of MCM-22 shows that the zeolite crystals are aligned forming a supra-crystallite structure of approximately 100 nm. The crystallites of MCM-22(12) seem to be organized in a more random fashion. The addition of TPOAC possibly causes the zeolite crystals to become separated, which is likely due to the hydrophobic nature of TPOAC grafted at the zeolite crystal surface. The random organization of the agglomerated crystallites results in interstitial voids that are in part responsible for the mesoporosity of the material. Furthermore, some crystallites show a decreased crystal size (inset Fig. 4b) pointing to the inhibiting effect of TPOAC on crystal growth. The TEM images show that some of the MWW layers of MCM-22(12) are separated due to the presence of TPOAC. In this way, additional interstitial voids were created, which contribute to the mesopore volume. The morphology of MCM-22(12)-pillared (Fig. 4c) is similar to that of MCM-22(12). The TEM image for ITQ-2 (Fig. 4d) confirms that this material contains single MWW layers.

$^{29}$Si MAS-NMR spectroscopy was employed to distinguish between the terminal silanol and framework silicate species. The amount of terminal silanol groups can be related to the external surface area. First, $^{1}H \rightarrow ^{29}Si$ cross-polarization (CP) measurements were conducted to prove the presence of Q3 ($Si(OSi)_3OH$ and Si(1Al)) and Q2 sites ($Si(OSi)_2(OH)_2$), next to the predominant Q4 sites ($SiO_4$). The Q2 sites are characterized by a peak at -93 ppm, while Q4 species are identified by overlapping peaks in the range of

-104 to -120 ppm [60]. Q3 species including $Si(OSi)_3OH$ and Si(1Al) are identified by peaks at -98 ppm and -101 ppm, respectively [60]. To quantify the various silicate species, the spectra were measured in high-power decoupling (hp-dec) mode (Fig. 5). The results of deconvolution of these spectra are given in Table 2. Hierarchical MCM-22 contains more Q3 species than bulk MCM-22 zeolite. As the Al bulk content is nearly the same for all MCM-22 zeolites, the higher Q3 concentration can be attributed to the higher silanol content and the larger external surface area. The larger external surface area is due to the inhibited crystal growth upon addition of TPOAC. It is consistent with the increasing fraction of Q2+Q3 species.

*Acidity characterization*

The Al coordination in the MCM-22 zeolites was determined by $^{27}Al$ MAS NMR spectroscopy. The spectra are shown in Fig. 6. The two peaks at 55 ppm (FAl1) and 48 ppm (FAl2) in the spectrum of MCM-22 indicate the presence of two types of framework Al species in line with the literature [60, 61]. The FAl1 species are located inside the micropores, while the FAl2 species reside at the external surface and/or the large cavities [61]. Another less pronounced feature at 0 ppm is due to extraframework aluminum (EFAl). The Al speciation was quantified by deconvolution of the $^{27}Al$ MAS NMR spectra (Table 2). The fraction of EFAl in MCM-22(12) is 30%, which is significantly higher than the EFAl content (21%) for MCM-22. After pillaring, MCM-22(12)-pillared contains a similar amount of EFAl. The addition of TPOAC led to a decrease in the FAl2 content for MCM-22(12) and MCM-22(12)-pillared, which we attribute to the change of the amount

of FAl species at the external surface. The removal of surface Al is also evident when the as-synthesized MCM-22 was delaminated to obtain ITQ-2. This phenomenon has already been reported for the synthesis of ITQ-2 [54, 58].

The $^{1}$H MAS NMR spectra help to characterize the various hydroxyl groups (Fig. 7). The bands at 1.9 ppm and 2.6 ppm are assigned to terminal hydroxyls associated with silanol groups and EFAL species, respectively [62]. The protons of the Brønsted acid sites (BAS) give rise to the 4.0 ppm peak in the $^{1}$H NMR spectrum. Internal silanols are characterized by the peak at 6.1 ppm. The content of the various hydroxyl species as determined from these NMR spectra are listed in Table 2. Comparing the quantitative data reveals the BAS content in MCM-22(12) to be lower than in MCM-22. After pillaring of MCM-22(12) the BAS concentration increased, indicated by the increase of the corresponding NMR signal. Further inspection of the NMR spectra suggests a decrease in EFAl content after pillarization of MCM-22(12), which is confirmed by the quantitative data. These observations are inconsistent with the findings from the $^{27}$Al MAS NMR experiments. Seemingly, a fraction of the EFAl is invisible to $^{27}$Al NMR [59, 63-66]. The larger BAS concentration of MCM-22(12)-pillared compared with MCM-22(12) is most likely due to leaching of the EFAl present upon acid treatment. In this way, part of the EFAl that was compensating the negative framework charge is removed, thus increasing the amount of BAS. The removal of FAl during delamination explains the lower BAS content of ITQ-2 as compared with the parent MCM-22. These findings are in agreement with the trends observed by $^{27}$Al MAS NMR spectroscopy and literature [58].

The acidic properties of the zeolites were characterized in more detail using FTIR spectroscopy. The spectra in Fig. 8 contain two main absorption bands at 3612 cm$^{-1}$ (BAS)

and 3749 $cm^{-1}$ (silanol groups). MCM-22(12) and MCM-22(12)-pillared contain more silanol groups than MCM-22, while the reverse holds for the BAS content. The silanol and BAS contents of ITQ-2 were comparable with MCM-22(12). The acidity of MCM-22(12)-pillared was larger than that of ITQ-2 and MCM-22(12), albeit lower than that of MCM-22. These findings are consistent with the results from $^{1}H$ MAS NMR results. Acid site quantification by FTIR spectroscopy after exposure of pyridine to the parent zeolites (Table 3) trends with the observations from the FTIR spectra and the $^{1}H$ MAS NMR results.

*Catalytic activity measurements: benzene alkylation with propene*

Fig. 9 depicts the time on stream behavior (Fig. 9a) and the selectivity (Fig. 9b) of the various MCM-22 zeolites and ITQ-2 in the liquid-phase alkylation of benzene with propylene. All catalysts initially show high activity, but deactivate with time on stream. ITQ-2 showed the highest stability in this reaction. The lower rate of deactivation of ITQ-2 as compared with MCM-22 is in line with previous reports [5]. The nano-crystalline MCM-22(12) exhibited better stability than the other MCM-22 materials, although the rate of deactivation is higher as compared with ITQ-2. The higher catalytic stability of ITQ-2 compared with bulk MCM-22 has been explained by the larger amount of BAS accessible to benzene at the external zeolite surface [5, 67, 68]. The deactivation of MCM-22 is usually attributed to carbonaceous deposits that cover these BAS at the external surface [69-71]. We attribute the lower rate of deactivation of MCM-22(12) compared with MCM-22 to the decreased crystallite size; the decreased crystallite size implies a higher external surface area and improved accessibility of benzene to the BAS at the external surface.

Moreover, the decrease of the diffusion path length will allow desorption of undesired products (oligomers, multiple alkylated aromatics) before they are converted into bulkier coke species. The stability towards deactivation of pillared MCM-22(12)-pillared was the lowest among the MCM-22 zeolites. This may be correlated with the higher acidity of this sample. Such deactivation has also been reported by the group of Corma [69], who showed that the selective deactivation of external BAS with 2,6-di-*tert*-butyl pyridine (DTPBPy) led to rapid decrease of the alkylation activity with time on stream. The explanation of low external BAS content of MCM-22(12)-pillared is supported by the lower selectivity to diisopropylbenzene (Fig. 9b) compared with MCM-22, MCM-22(12) and ITQ-2. The selectivity to multi-alkylated benzenes products is higher for MWW zeolites with a higher external surface area [67, 71]. The lower external acidity of MCM-22(12)-pillared due to silica deposition explains the lower selectivity to diisopropylbenzene.

3.2 Preparation, characterization and catalytic testing of bifunctional Mo/zeolites.

The various MCM-22 zeolites were also used as acid supports for the preparation of Mo-modified zeolite catalysts for the MDA reaction. The Mo was introduced by incipient wetness impregnation followed by calcination. The final Mo loading was close to the targeted Mo content of 4 wt% (see Table 3).

*Characterization of bifunctional Mo/zeolites catalysts*

The acidity of the Mo-modified zeolites was determined by pyridine adsorbed FTIR (see Table 3). Modification of the parent materials with Mo led to a decrease in acidity for all samples. The decrease in acidity is due to exchange of the protons associated to the BAS

with Mo-oxo species. Silylation led to further decrease of the acidity in agreement with an earlier report for Mo/ZSM-5 [73]. The acidity decrease in this case can be attributed to the improved spreading of Mo over the zeolite and to the deactivation of the external acid sites by the silylation treatment.

*Catalytic activity measurements: methane dehydroaromatization*

The time on stream behavior of the Mo/zeolites is shown in Fig. 10. While the methane conversion decreased with time on stream (Fig. 10a), the benzene selectivity exhibits an optimum around 4 h. The initially low benzene selectivity relates to the conversion of some residual Mo-oxide in the precarburized catalyst into Mo-carbide. The highest benzene selectivity (55 wt%) was observed for Mo/MCM-22(12) after 4 h on stream. The benzene selectivities for Mo/MCM-22 and Mo/MCM-22(12)-pillared were lower (~40 wt%). Mo/ITQ-2 showed the lowest benzene selectivity (~30 wt%). The higher benzene selectivity of Mo/MCM-22 compared to Mo/ITQ-2 is in keeping with previous findings [58]. The benzene selectivity inversely correlates with the coke selectivity. Several reports have discussed the formation of coke at the external surface BAS as the most likely reason for MDA catalyst deactivation [74-77]. Deactivation of these external surface BAS by the addition of a small amount of silica has been shown to improve benzene selectivity [73]. Therefore, we evaluated to what extent the performance of these materials can be improved by silylation with TEOS. The methane conversion as a function of time on stream did not change upon silylation. Silylation also did not affect the selectivities (Figs. 11b and 11c) for Mo/MCM-22(12), Mo/MCM-22(12)-pillared and Mo/ITQ-2 upon silylation. However, the benzene selectivity of Mo/MCM-22 strongly improved by silylation. We surmise that

the less pronounced effect of silylation on nano-crystalline MCM-22 and ITQ-2 is due to their much higher silanol content.

We also evaluated the usefulness of an earlier developed reaction/regeneration cycle procedure for the MDA reaction [78]. A typical reaction/regeneration cycle consisted of reaction for 1.5 h at 973 K, followed by an oxidation step in artificial air at 773 K. Cooling was done in inert atmosphere but the reaction temperature was recovered by heating in the feed mixture. The results are shown in Fig. 12 (each data point represents catalytic performance 70 min after the regeneration cycle). These data point out the increased stability and benzene selectivity of silylated Mo/MCM-22, consistent with the data in Fig. 10 and 11. Both silylated and non-silylated Mo/MCM-22 displayed increased benzene selectivity with each consecutive regeneration cycle. The methane conversion increased during the first 3 reaction/regeneration cycles. Thereafter, a small decrease in the methane conversion can be noted. Acidity characterization (Table 3) on the calcined Mo/MCM-22 and Mo/MCM-22(Si) catalysts after exposure of 12 consecutive reaction cycles reveals a substantial loss in acidity (~-60%) compared to the fresh catalyst. The reason for this is not clear, but possibly the loss of the integrity of the zeolite structure, ineffective removal of refractory coke or agglomeration of the Mo-phase during the oxidative regeneration step may provide an explanation [79].

## 4. Conclusions

A one-pot synthesis procedure for the preparation of nano-crystalline MCM-22 was developed. It involves the addition of an amphiphilic organosilane to the synthesis gel. The total Brønsted acidity of this nano-crystalline MCM-22 zeolite is lower than that of bulk

MCM-22. Nevertheless, nano-crystalline MCM-22 shows higher catalytic performance in the liquid-phase alkylation of benzene with propylene due to the increased accessibility of the Brønsted acid sites. The low mechanical stability of the hierarchical material was improved by pillaring as followed from textural analysis before and after exerting mechanical forces by pelletizing the powdered zeolite. The addition of silica during the pillaring with TEOS led to a substantial decrease of the acidity and the catalytic alkylation performance. The shorter diffusion pathways through the MCM-22 with reduced crystal size also led to an improved benzene selectivity in the methane aromatization reaction. External surface modification of the hierarchical Mo/MCM-22 catalyst following a silylation treatment was detrimental to the catalytic performance of this catalyst in MDA.

*Acknowledgements*

Funding from the 7th Framework Program of the European Commission through the Collaborative Project Next-GTL (agreement n° 229183) and financial support by the Spanish Government-MINECO through "Severo Ochoa" (SEV 2012-0267), Consolider Ingenio 2010-Multicat and MAT2012-31657 are acknowledged. Marta E. Martínez Armero thanks MINECO for economical support through pre-doctoral fellowship for doctors training (BES-2013-066800). The authors thank B. Esparcia for technical assistance.

References


[1] M.E. Leonowicz, J.A. Lawton, S.L. Lawton, M.K. Rubin, Science 264 (1994) 1910-1913.
[2] W.O. Haag, R.M. Lago, P.B. Weisz, Faraday Discuss. 72 (1981) 317-330.
[3] A. Corma, C. Corell, F. Llopis, A. Martinez, J. Pérez-Pariente, Appl. Catal., A 115 (1994) 121-134.
[4] R. Ravishankar, S. Sivasanker, Appl. Catal., A 142 (1996) 47-59.
[5] P.J. Van den Brink, A. Corma, E.J. Creyghton, V. Fornes, V. Martines-Soria, WO patent 01/21562, 2001.
[6] C. Flego, G. Pazzuconi, E. Bencini C. Perego, Stud. Surf. Sci. Catal. 126 (1999) 461-464.
[7] C. Perego, S. Amarilli, R. Millini, G. Bellussi, G. Girotti, G. Terzoni, Microporous Mesoporous Mater. 6 (1996) 395-404.
[8] Y. Shu, D. Ma, L. Xu, Y. Xu, X. Bao, Catal. Lett. 70 (2000) 67-73.
[9] N. Chu, J. Yang, J. Wang, S. Yu, J. Lu, Y. Zhang, D. Yin, Catal. Comm. 11 (2010) 513-517.
[10] S.L. Lawton, M.E. Leonowicz, R.D. Partridge, P. Chu, M.K. Rubin, Microporous Mesoporous. Mater. 23 (1998) 109-117.
[11] C.T. Kresge, Q.N. Le, W.J. Roth, R.T. Thompson, U.S. Patent 5,259,565, 1993.
[12] P. Chu, M.E. Landis, Q.N. Le, U.S. Patent 5,334,795, 1994.
[13] D.L. Holtermann, R. Innes, U.S. Patent 5,149,894, 1992.
[14] M.F. Bentham, G.J. Gajda, R.H. Jensen, H.A. Zinnen, Erdöl Erdgas Kohle 113 (1997) 84-88.
[15] G. Sastre, C. Richard, A. Catlow, A Corma, J. Phys. Chem. B 103 (1999) 5187-5196.
[16] A. Corma, V. Fornes, S.B. Pergher, Th.L.M. Maesen, J.G. Buglass, Nature 396 (1998) 353-356.
[17] A. Corma, V. Fornés, J.M. Guil, S. Pergher, Th. L. M. Maesen, J.G Buglass, Microporous Mesoporous Mater. 38 (2000) 301-309.
[18] L. Wang, L. Tao, M. Xie, G. Xu, Catal. Lett. 21 (1993) 35-41.
[19] Y. Shu, D. Ma, L. Xu, Y. Xu, X. Bao, Catal. Lett. 70 (2000) 67-73.
[20] V.T.T. Ha, L.V. Tiep, P. Meriaudeau, C. Naccache, J. Mol. Catal., A 181 (2002) 283-290.
[21] M.T. Portilla, F.J. Llopis, C. Martínez, S. Valencia, A. Corma, Appl. Catal., A 393 (2011) 257-268.
[22] L. Chen, L. Lin, Z.S. Xu, X.S. Li, T. Zhang, J. Catal. 157 (1995) 190–200.
[23] S. Liu, L. Wang, R. Ohnishi, M. Ichikawa, Kinet. Catal. 41 (2000) 132–144.
[24] B.M. Weckhuysen, M.P. Rosynek, J.H. Lunford, Catal. Lett. 52 (1998) 31–36.
[25] D. Ma, D. Wang, L. Su, Y. Shu, Y. Xu, X. Bao, J. Catal. 208 (2002) 260–269.
[26] C. Descorme, P. Gelin, C. Lecuyer, A. Primet, Appl. Catal., B 13 (1997) 185–195.
[27] L. Su, L. Liu, J. Zhuang, H. Wang, Y. Li, W. Shen, Y. Xu, X. Bao, Catal. Lett. 91 (2003) 155-166.
[28] A. Martinez, E. Peris, M. Derewinski, A. Burkat-Dulak, Catal. Today 169 (2011) 75-84.

[29] N.B. Chu, J.Q. Wang, Y. Zhang, J.H. Yang, J.M. Lu, D.H. Yin, Chem. Mater. 22 (2010) 2757-2763.
[30] S. van Donk, A. H. Janssen, J. H. Bitter and K. P. de Jong, Catal. Rev. Sci. Eng., 45 (2003) 297–319.
[31] J. Pérez-Ramírez, C.H. Christensen, K. Egeblad, C.H. Christensen, J.C. Groen, Chem. Soc. Rev. 37 (2008) 2530-2542.
[32] D.P. Serrano, J.M. Escola, P. Pizarro, Chem. Soc. Rev. 42 (2013) 4004-4035.
[33] S. Morin, P. Ayrault, N.S. Gnep, M. Guisnet, Appl. Catal., A 166 (1998) 281-292.
[34] J. Lynch, F. Raatz, C. Delande, Stud. Surf. Sci. Catal. 39 (1987) 547-557.
[35] J. Lynch, F. Raatz, P. Dufresne, Zeolites 7 (1987) 333-340.
[36] V. Patzelova, N.I. Jaeger, Zeolites 7 (1987) 240-242.
[37] A. Zukal, V. Patzelova, U. Lohse, Zeolites 6 (1986) 133-136.
[38] Y. Sasaki, T. Suszuki, Y. Takamura, A. Saji, H. Saka, J. Catal. 178 (1998) 94-100.
[39] C. Choi-Feng, J.B. Hall, B.J. Huggins, R.A. Beyerlein, J. Catal. 140 (1993) 395-405.
[40] R.A. Beyerlein, C. Choi-Feng, J.B. Hall, B.J. Huggins, G.J. Ray, Top. Catal. 4 (1997) 27-42.
[41] M. Choi, H. S. Cho, R. Srivastava, C. Venkatesan, D.-H. Choi, R. Ryoo, Nat. Mater., 5 (2006) 718–723.
[42] K.T.G. Carvalho, E.A. Urquieta-Gonzalez., Catal. Today 243 (2015) 92-102.
[43] G.R. Meima, Cattech 2 (1998) 5-12.
[44] P. Hudec, J. Novansky, S. Silhar, T.N. Trung, M. Zubek, J. Madar, J. Ads. Sci. Tech. 3 (1986) 159-166.
[45] B.L. Meyers, T.H. Fleisch, G.J. Ray, J.T. Miller, J.B. Hall, J. Catal. 110 (1988) 82-95.
[46] M. Tromp, J.A. van Bokhoven, M.T. Garriga Oostenbrink, J.H. Bitter, K.P. de Jong, D.C. Koningsberger, J. Catal. 190 (2000) 209-214.
[47] J.C. Groen, W. Zhu, S. Brouwer, S.J. Huynink, F. Kapteijn, J.A. Moulijn, J. Pérez-Ramírez, J. Am. Chem. Soc. 129 (2007) 355–360.
[48] J. C. Groen, L. A. A. Peffer, J. A. Moulijn and J. Pérez-Ramírez, J. Mater. Chem. 16 (2006) 2121-2131.
[49] C. J. H. Jacobsen, C. Madsen, J. Houzvicka, I. Schmidt and A. Carlsson, J. Am. Chem. Soc. 122 (2000) 7116–7117.
[50] K. Zhu, K. Egeblad and C. H. Christensen, Eur. J. Inorg. Chem. 25 (2007) 3955–3960
[51] A.H. Janssen, I. Schmidt, C.J.H. Jacobsen, A.J. Koster, K.P. De Jong, Microporous Mesoporous Mater. 65 (2003) 59-75.
[52] J.Yang, J. Chu, J. Wang, D. Yin, J. Lu, Y. Zhang, Chin. J. Catal. 35 (2014) 49-57.
[53] I. Güray, J. Warzywoda, N. Baç, A. Sacco, Microporous Mesoporous Mater. 31 (1999) 241–251.
[54] A. Corma, U. Diaz, V. Fornés, J.M. Guil, J. Martínez-Triguero, E.J. Creyghton, J. Catal. 191 (2000) 218-224.
[55] S. Inagaki, K. Kamino, E. Kikuchi, M. Matsukata, App. Catal., A 318 (2007) 22-27.
[56] M. Cheng, D. Tan, X. Bao, Chem. Comm. (2000) 1713-1714.

[57] A. Corma, C. Corell, J. Peréz-Pariente, J.M. Guil, R. Guil-Lopéz, S. Nicolopoulos, J. Gonzalez Calbet, M. Vallet-Regi, Zeolites 16 (1996) 7-14.
[58] A. Martínez, E. Peris, G. Sastre, Catal. Today 107-108 (2005) 676-684.
[59] Y.J. He, G.S. Nivarthy, F. Eder, K. Seshan, J.A. Lercher, Microporous Mesoporous Mater. 25 (1998) 207-224.
[60] W. Kolodziejski, C. Zocovich-Wilson, C. Corell, J. Pérez-Pariente, A. Corma, J. Phys. Chem. 99 (1995) 7002-7008.
[61] P. Mériaudeau, A. Tuel, T.T.H. Vu, Catal. Lett. 61 (1999) 89-92.
[62] M. Hunger, S. Ernst, S. Steuernagel, J. Weitkamp, Microporous Mater. 6 (1996) 349-353.
[63] E. Brunner, H. Ernst, D. Freude, T. Fröhlich, M. Hunger, H. Pfeifer, J. Catal. 127 (1991) 34-41.
[64] S.M. Campbell, D.M. Bibby, J.M. Coddington, R.F. Howe, R.H. Meinhold, J. Catal. 161 (1996) 338-349.
[65] A. Maijanen, E.G. Derouane, J.B. Nagy, Appl. Surf. Sci. 75 (1994) 204-212.
[66] C.A. Fyfe, J.L. Bretherton, L.Y. Lam, J. Am. Chem. Soc. 123 (2001) 5285-5291.
[67] C. Perego, P. Ingallina, Green Chem. 6 (2004) 274-2794.
[68] A. Corma, Nature 396 (1998) 353-356.
[69] A. Corma, V. Martínez-Soria, E. Schnoeveld, J. Catal. 192 (2000) 163–173.
[70] C. Perego, S. Amarilli, R. Millini, G. Bellussi, G. Gerotti, G. Terzoni, Microporous Mesoporous Mater. 6 (1996) 395-404.
[71] J. Rigoreau, S. Laforge, N.S. Gnep, M. Guisnet, J. Catal. 236 (2005) 45-54.
[72] J.C. Cheng, T. F. Degnan, J.S. Beck, Y.Y. Huang, M. Kalyanaraman, J.A. Kowalasky, C.A. Loehr and D.N. Mazzone, Stud. Surf. Sci. Catal. 121 (1999) 53-60.
[73] C.H.L. Tempelman, V.O. de Rodrigues, E.R.H van Eck, P.C.M.M. Magusin, E.J.M. Hensen, Microporous Mesoporous Mater. 259 (2015) 259-273.
[74] H. Liu, L. Su, H. Wang, W. Shen, X. Bao, Y. Xu, Appl. Catal. A, 236 (2002) 263-280.
[75] J. Bai, S. Liu, S. Xie, L. Xu, L. Lin, Stud. Surf. Sci. Catal. 147 (2004) 715-720.
[76] X. Dong, Y. Song, W. Lin, Catal. Commun. 8 (2007) 539-542.
[77] C.H.L. Tempelman, E.J.M. Hensen, App. Catal. B 176-177 (2015) 731-739.
[78] M.T. Portilla, F.J. Llopis, C. Martinez, Catal. Sci. Technol. (2015), DOI: 10.1039/C5CY00356C .
[79] H. Ma, R. Kojima, R. Ohnishi, M. Ichikawa, Appl. Catal., A 275 (2004) 183–187.

**Figure captions**

**Figure 1:** Wide angle XRD reflection patters of calcined (a) MCM-22, (b) MCM-22(120) (c) MCM-22(12), (d) MCM-22(6), (d) MCM-22(12)-pillared and ITQ-2.

**Figure 2:** Ar physisorption isotherms of (square) MCM-22, (circle) MCM-22(12), (triangle) MCM-22(12)-pillared and (diamond) ITQ-2. Isotherms with open symbols correspond to samples measured after exposing to external mechanical force. The isotherms are presented in a stacked fashion for clarity. The Y offsets are progressively increased with 100 $cm^3/g$ for each subsequent sample.

**Figure 3:** TEM micrographs of (a) MCM-22, (b) MCM-22(12), (c) MCM-22(12)-pillared and (d) ITQ-2.

**Figure 4:** SEM micrographs of (a) MCM-22, (b) MCM-22(12), (c) MCM-22(12)-pillared and (d) ITQ-2.

**Figure 5:** $^{29}Si$ MAS NMR spectra measured in hp-dec mode of (a) MCM-22, (b) MCM-22(12), (c) MCM-22(12)-pillared and (d) ITQ-2.

**Figure 6:** $^{27}Al$ MAS NMR spectra of (a) MCM-22, (b) MCM-22(12), (c) MCM-22(12)-pillared and (d) ITQ-2.

**Figure 7:** $^{1}H$ MAS NMR spectra of (a) MCM-22, (b) MCM-22(12), (c) MCM-22(12)-pillared and (d) ITQ-2.

**Figure 8:** FTIR spectra of (a) MCM-22, (b) MCM-22(12), (c) MCM-22(12)-pillared and (d) ITQ-2 (samples dehydrated in vacuo at 723 K).

**Figure 9:** Catalytic performance in benzene alkylation (T = 398 K; 3.5 MPa; 1/3.5 (mol/mol) Benzene/propylene): (a) propylene conversion and (b) cumene (closed symbols) and diisopropylbenzene (open symbols) selectivities of MCM-22 (■), MCM-22(12) (●), MCM-22(12)-pillared (▲) and ITQ-2 (▼).

**Figure 10:** Catalytic performance in methane dehydroaromatization (T = 973 K; 0.1 MPa; 5/95 (v/v) $N_2/CH_4$): (a) methane conversion, (b) benzene (closed symbols) and naphthalene (open symbols) selectivities and (c) coke (closed symbols) and olefin (open symbols) selectivities of MCM-22 (■), MCM-22(12) (●), MCM-22(12)-pillared (▲) and ITQ-2 (♦).

**Figure 11:** Catalytic performance in methane dehydroaromatization (T = 973 K; 0.1 MPa; 5/95 (v/v) $N_2/CH_4$): (a) methane conversion, (b) benzene (closed symbols) and naphthalene (open symbols) selectivities and (c) coke (closed symbols) and olefin (open symbols) selectivities of silylated MCM-22 (■), MCM-22(12) (●), MCM-22(12)-pillared (▲) and ITQ-2 (♦).

**Figure 12:** Catalytic performance in methane dehydroaromatization with intermediate regeneration ((T = 973 K; 0.1 MPa; 5/95 (v/v) $N_2/CH_4$); each point represents a time on stream of 70 min): (a) methane conversion, (b) benzene (square) and naphthalene (circle) selectivities and (c) coke (square) and olefin (circle) selectivities of non-silylated (closed symbols) and silylated (open symbols) MCM-22.

**Tables and figures**

Table 1: Physico-chemical properties and elemental composition of the materials before and after applying external pressure.

| Sample | HMI/TPOAC | Si/Al[1] | Si/Al[2] | Pressure[3] ($10^6$ N/m$^2$) | $V_{micro}$ (cm$^3$/g) | $V_{meso}$ (cm$^3$/g) | $S_{micro}$ (m$^2$/g) | $S_{meso}$ (m$^2$/g) | $S_{BET}$ (m$^2$/g) | $\Delta V_{meso}$ (%) |
|---|---|---|---|---|---|---|---|---|---|---|
| MCM-22 | ∞ | 16.3 | 19.2 | 0 | 0.15 | 0.08 | 332 | 54 | 449 | - |
| | ∞ | 16.3 | 19.2 | 16 | 0.10 | 0.09 | 191 | 54 | 308 | +12 |
| MCM-22(120) | 120 | 16.3 | - | 0 | 0.14 | 0.18 | 263 | 95 | 370 | - |
| MCM-22(12) | 12 | 16.3 | 20.6 | 0 | 0.13 | 0.31 | 184 | 122 | 359 | - |
| | 12 | 16.3 | 20.6 | 16 | 0.04 | 0.18 | 94 | 94 | 219 | -40 |
| MCM-22(12)-pillared | 12 | 16.3 | 21.5 | 0 | 0.05 | 0.32 | 126 | 182 | 406 | - |
| | 12 | 16.3 | 21.5 | 16 | 0.05 | 0.26 | 118 | 145 | 347 | -16 |
| ITQ-2 | ∞ | 16.3 | 23.7 | 0 | 0.14 | 0.26 | 294 | 160 | 708 | - |

[1] Ratio of Si/Al in the synthesis gel.
[2] Determined from ICP-AES elemental analysis.
[3] Pressure was applied for 60 s.

Table 2: Relative contributions of Si, Al and H species in the MWW zeolites as determined by deconvolution of $^{29}Si$, $^{27}Al$ and $^{1}H$ MAS NMR spectra.

| Nucleus | $^{29}Si$ NMR | | | $^{27}Al$ NMR | | | $^{1}H$ NMR | | | |
|---|---|---|---|---|---|---|---|---|---|---|
| Sample | Q4 (%) | Q3 (%) | Q2 (%) | FAl1 (%) | FAl2 (%) | EFAl (%) | $SiOH_{ext}$ (a.u) | $SiOH_{int}$ (a.u) | Si(OH)Al (a.u) | EFAlOH (a.u) |
| MCM-22 | 92 | 7 | 1 | 67 | 12 | 21 | 25 | 22 | 44 | 7 |
| MCM-22(12) | 84 | 15 | 1 | 62 | 8 | 30 | 49 | 13 | 26 | 17 |
| MCM-22(12)-pillared | 82 | 16 | 2 | 61 | 7 | 32 | 63 | 29 | 39 | 10 |
| ITQ-2 | 79 | 19 | 2 | 73 | 6 | 21 | 52 | 19 | 36 | 14 |

Table 3: Acidic properties of parent and Mo-modified MWW zeolites as determined by pyridine adsorbed FTIR spectroscopy.

| Sample | Catalyst treatment[1] | Mo[2] (wt%) | $Py_{ads}$ IR[3] | | | | | |
|---|---|---|---|---|---|---|---|---|
| | | | $BAS_{523}$ (a.u.) | $BAS_{623}$ (a.u.) | $BAS_{673}$ (a.u.) | $LAS_{523}$ (a.u.) | $LAS_{623}$ (a.u.) | $LAS_{673}$ (a.u.) |
| MCM-22 | Fresh | - | 299 | 101 | 176 | 68 | 168 | 128 |
| Mo/MCM-22 | Fresh | 3.5 | 166 | 74 | 110 | 36 | 47 | 44 |
| | SR | 3.9 | 122 | 85 | 75 | 64 | 41 | 51 |
| | RC | 4.3 | 66 | 54 | 40 | 41 | 18 | 29 |
| Mo/MCM-22(Si) | Fresh | 3.4 | 154 | 76 | 108 | 65 | 57 | 59 |
| | SR | 3.8 | 125 | 83 | 84 | 69 | 56 | 62 |
| | RC | 3.9 | 64 | 71 | 32 | 50 | 27 | 45 |
| MCM-22(12) | Fresh | - | 128 | 66 | 120 | 86 | 64 | 58 |
| Mo/MCM-22(12) | Fresh | 3.7 | 110 | 52 | 94 | 58 | 49 | 45 |
| Mo/MCM-22(12, Si) | Fresh | 3.3 | 129 | 78 | 64 | 33 | 37 | 56 |
| MCM-22(12)-pillared | Fresh | - | 190 | 149 | 145 | 129 | 97 | 137 |
| Mo/MCM-22(12)-pillared | Fresh | 3.7 | 110 | 71 | 77 | 54 | 36 | 46 |
| Mo/MCM-22(12, Si)-pillared | Fresh | 3.3 | 99 | 58 | 55 | 43 | 55 | 33 |
| ITQ-2 | Fresh | - | 190 | 133 | 131 | 117 | 33 | 103 |
| Mo/ITQ-2 | Fresh | 3.9 | 168 | 79 | 123 | 67 | 65 | 47 |
| Mo/ITQ-2(Si) | Fresh | 3.8 | 130 | 64 | 80 | 49 | 44 | 44 |

[1] State of the catalyst. (Fresh = Fresh catalyst, SR = catalyst calcined after single run in MDA of 19 h, RC = catalyst calcined after 12 consecutive MDA reaction/regeneration cycles)
[2] Determined by ICP-AES measurements.
[3] Determined by IR spectroscopy of pyridine.

Figure 1

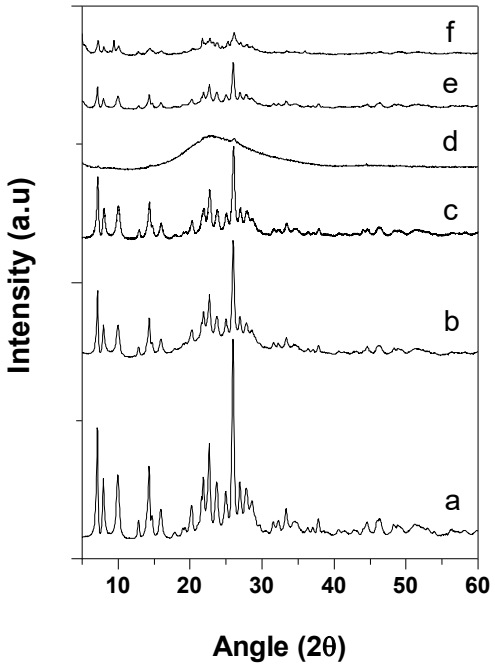

Figure 2

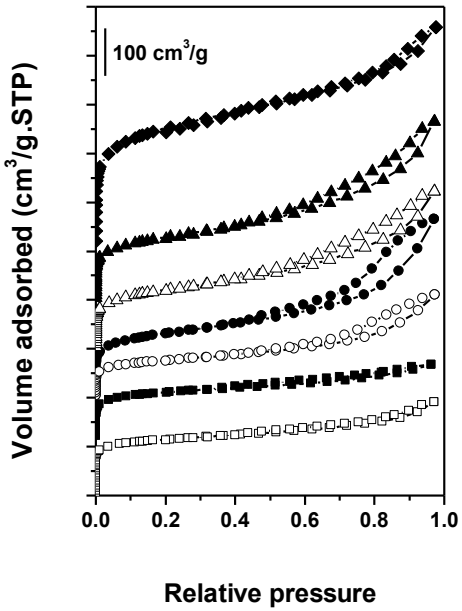
100 cm3/g
Volume adsorbed (cm3/g.STP)
0.0
0.2
0.4
0.6
0.8
1.0
Relative pressure

Figure 3

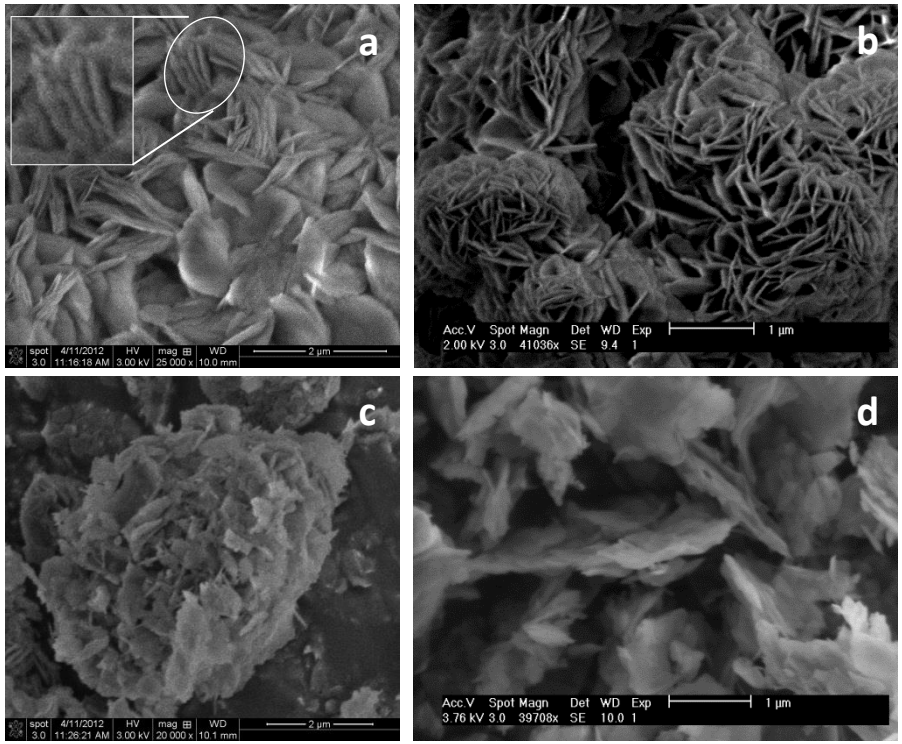
a
spot 3.0 | 4/11/2012 11:16:18 AM | HV 3.00 kV | mag 25 000 x | WD 10.0 mm | 2 µm
b
Acc.V Spot Magn Det WD Exp 1 µm
2.00 kV 3.0 41036x SE 9.4 1
c
spot 3.0 | 4/11/2012 11:26:21 AM | HV 3.00 kV | mag 20 000 x | WD 10.1 mm | 2 µm
d
Acc.V Spot Magn Det WD Exp 1 µm
3.76 kV 3.0 39708x SE 10.0 1

Figure 4

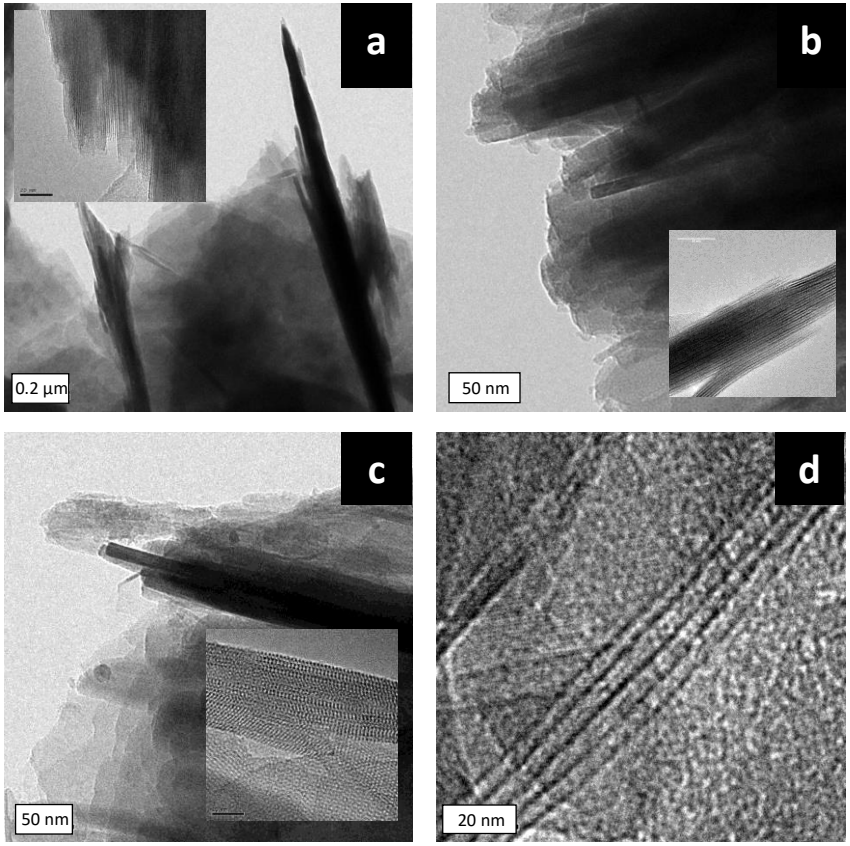

Figure 5

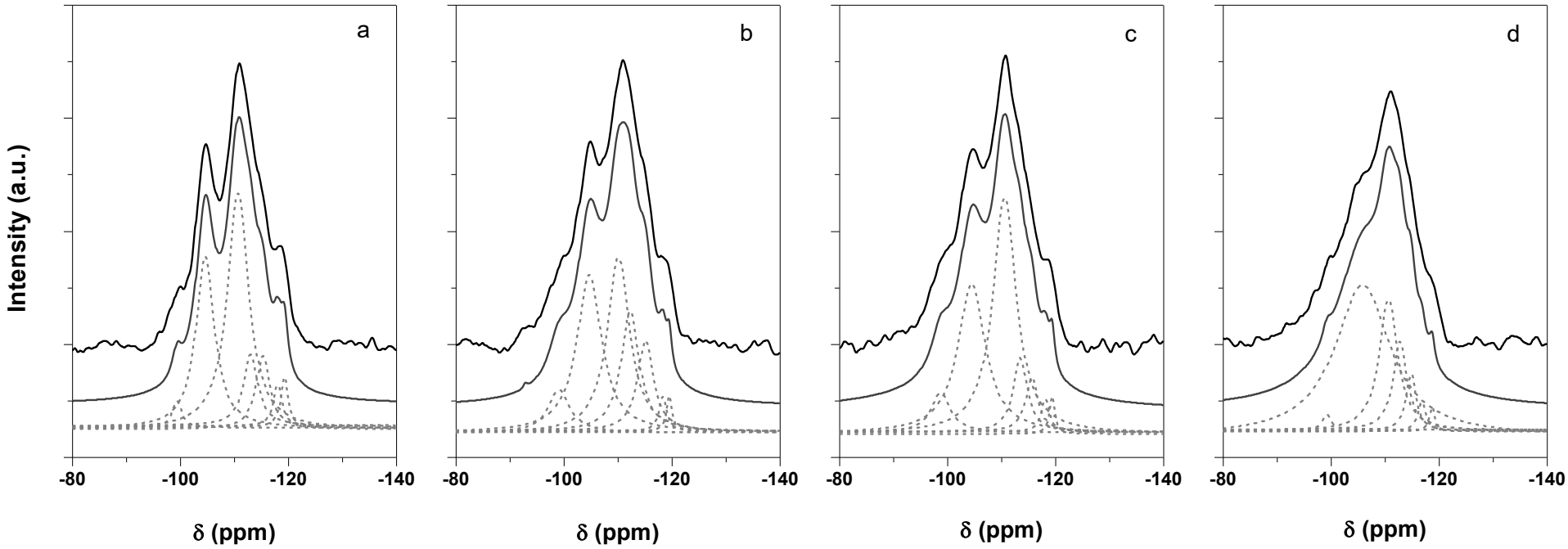

Figure 6

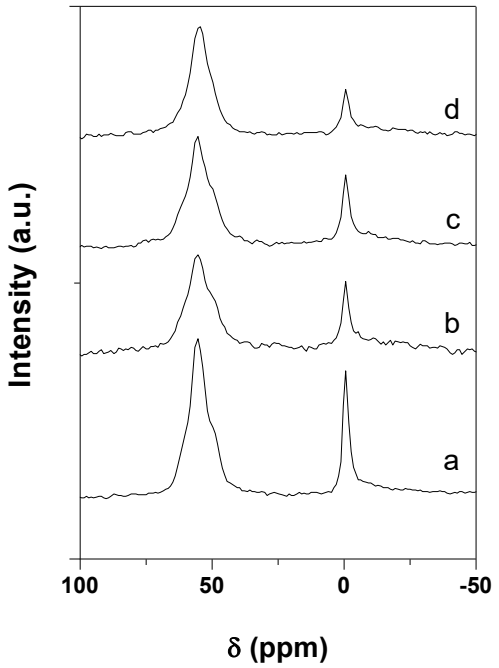

Figure 7

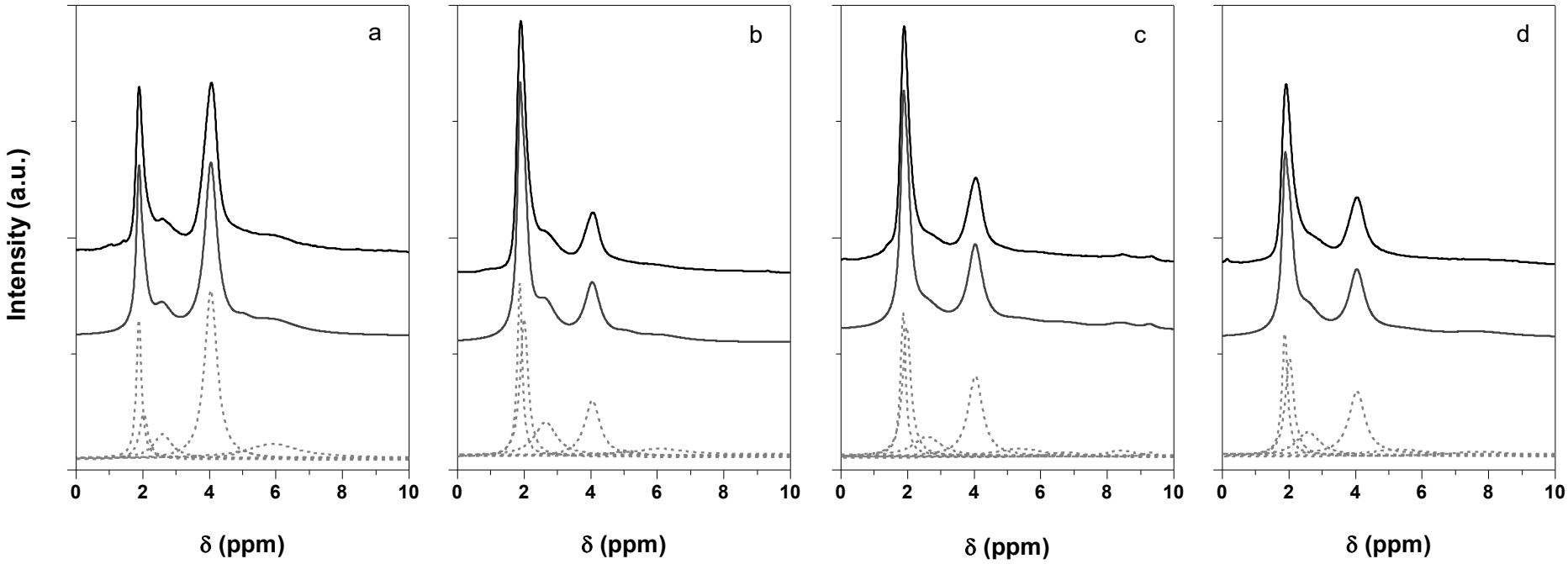

Figure 8

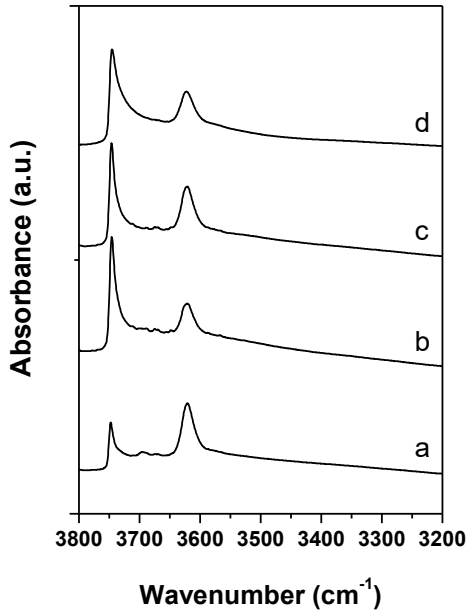
Absorbance (a.u.)
d
c
b
a
3800 3700 3600 3500 3400 3300 3200
Wavenumber (cm-1)

Figure 9

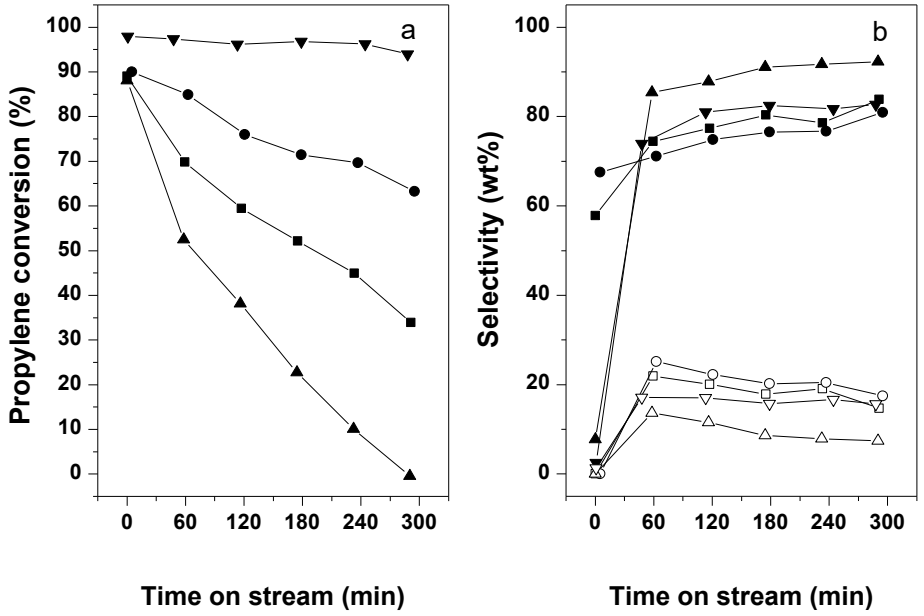
a
b
Propylene conversion (%)
Selectivity (wt%)
Time on stream (min)
Time on stream (min)
0
10
20
30
40
50
60
70
80
90
100
0
20
40
60
80
100
0
60
120
180
240
300

Figure 10

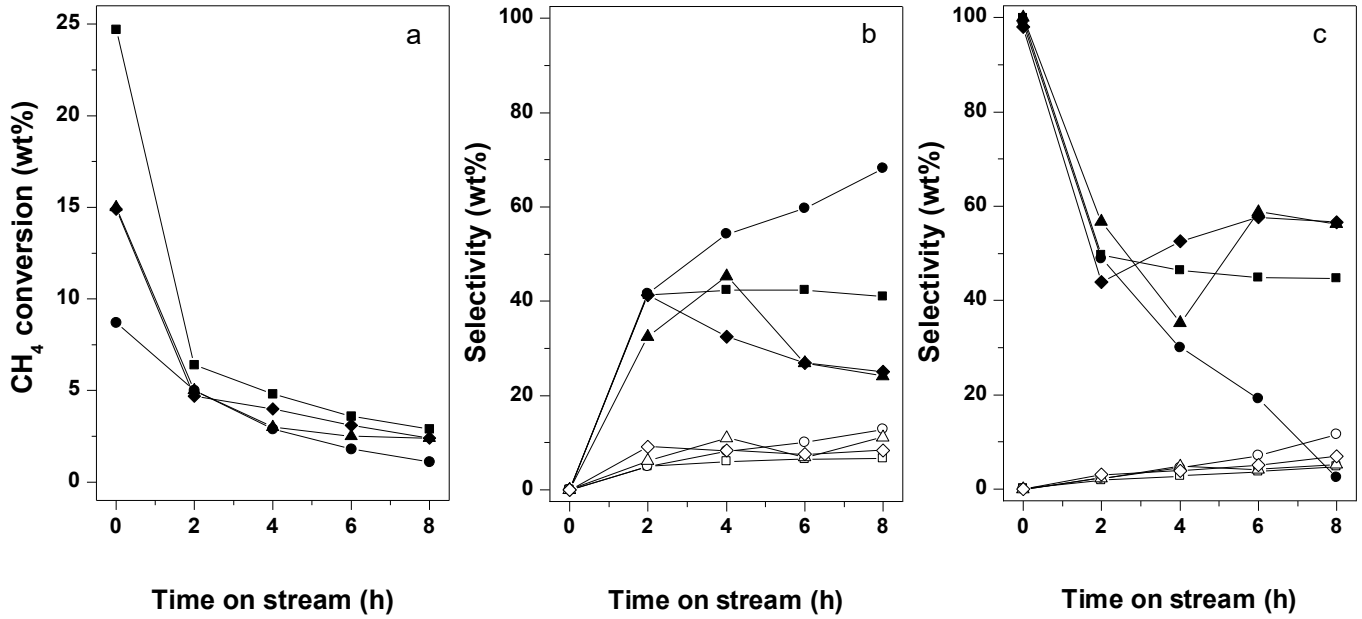
a
b
c
$CH_4$ conversion (wt%)
Selectivity (wt%)
Selectivity (wt%)
Time on stream (h)
Time on stream (h)
Time on stream (h)
0
5
10
15
20
25
0
20
40
60
80
100
0
20
40
60
80
100
0
2
4
6
8

Figure 11

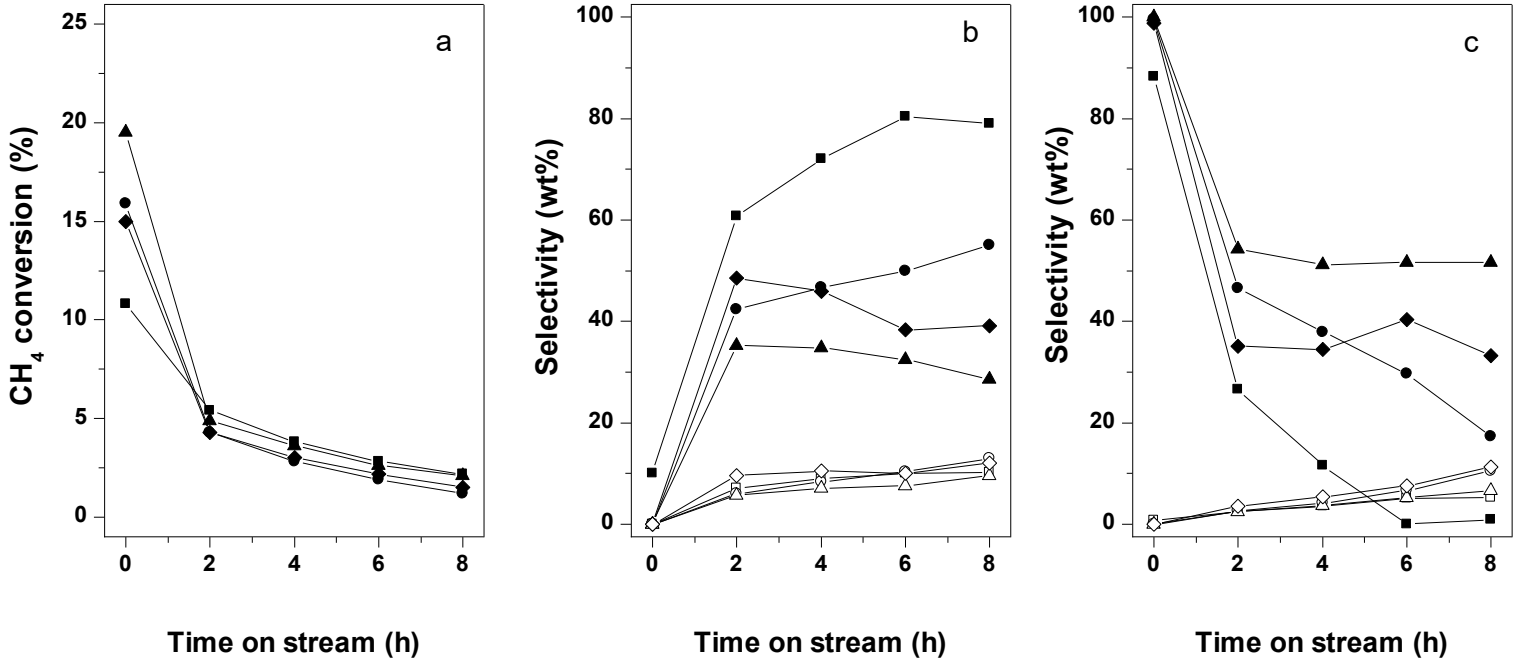
a
b
c
$CH_4$ conversion (%)
Selectivity (wt%)
Selectivity (wt%)
Time on stream (h)
Time on stream (h)
Time on stream (h)
0
5
10
15
20
25
0
20
40
60
80
100
0
20
40
60
80
100
0
2
4
6
8

Figure 12

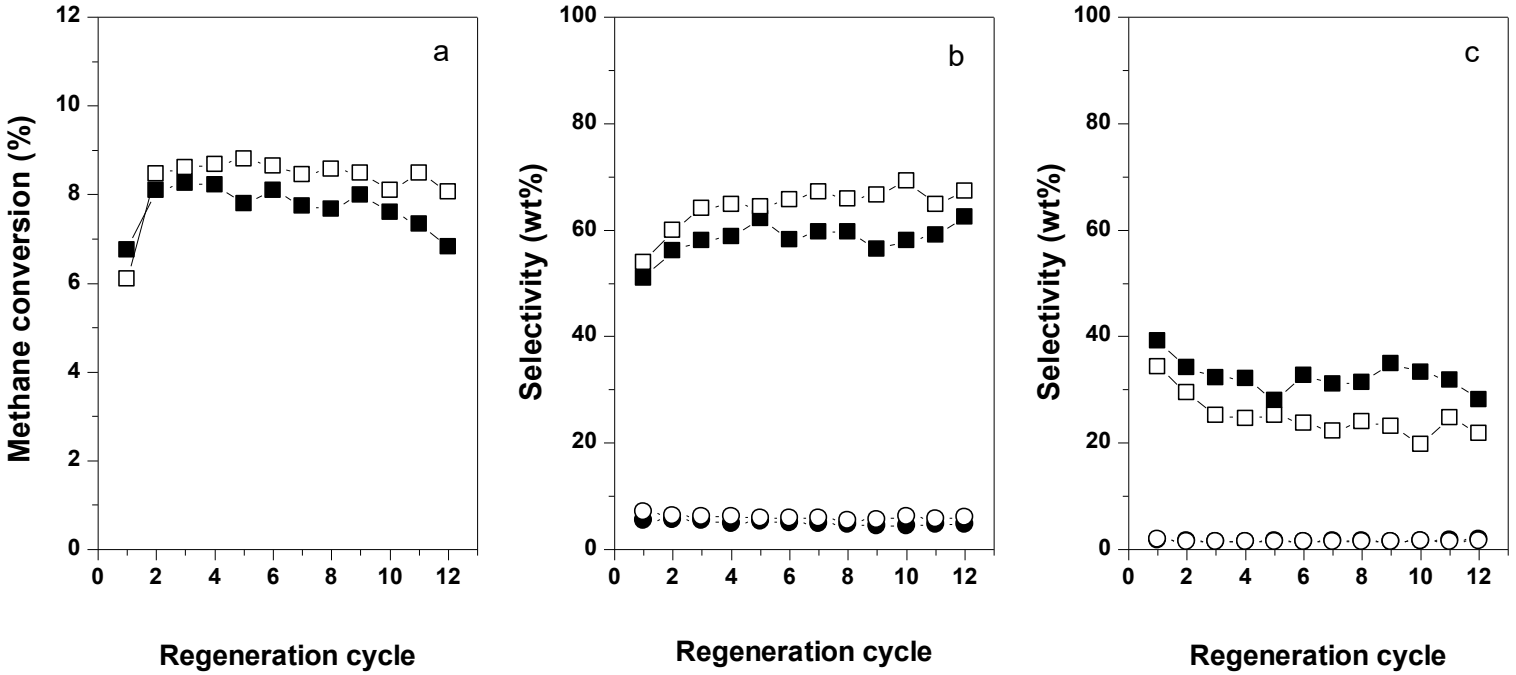
a
Methane conversion (%)
Regeneration cycle
b
Selectivity (wt%)
Regeneration cycle
c
Selectivity (wt%)
Regeneration cycle